Research Article **Open Access**

Self-assembly Stability Compromises the Efficacy of Tryptophan-Containing Designed Anti-measles Virus Peptides

Diogo A. Mendonça[1], Tiago N. Figueira[1], Manuel N. Melo[2], Olivia Harder[3], Stefan Niewiesk[3], Anne Moscona[4,5,6,7], Matteo Porotto[4,5,8*] and Ana Salomé Veiga[1*]

[1]Instituto de Medicina Molecular, Faculdade de Medicina, Universidade de Lisboa, 1649-028 Lisboa, Portugal
[2]Instituto de Tecnologia Química e Biológica António Xavier, Universidade Nova de Lisboa, 2775-412 Oeiras, Portugal
[3]Department of Veterinary Biosciences, College of Veterinary Medicine, The Ohio State University, Columbus, Ohio 43210, United States of America
[4]Department of Pediatrics, Columbia University Medical Center, New York 10032, United States of America
[5]Center for Host-Pathogen Interaction, Columbia University Medical Center, New York 10032, United States of America
[6]Department of Microbiology & Immunology, Columbia University Medical Center, New York 10032, United States of America
[7]Department of Physiology & Cellular Biophysics, Columbia University Medical Center, New York 10032, United States of America
[8]Department of Experimental Medicine, University of Study of Campania 'Luigi Vanvitelli', 81100 Caserta, Italy

Abstract

The resurgence of several infectious diseases, like measles, has driven the search for new chemotherapeutics to prevent and treat viral infections. Self-assembling antiviral peptides are a promising class of entry inhibitors capable of meeting this need. Fusion inhibitory peptides derived from the heptad repeat of the C-terminal (HRC) of the measles fusion protein, dimerized and conjugated with lipophilic groups, were found to be efficacious against measles virus. The structures of the self-assembled nanoparticles formed by these peptides modulated their activity. Based on the analysis of a L454W mutation in the fusion protein of a naturally occurring measles viral isolate, HRC peptides bearing the tryptophan residue at position 454 (HRC-L454W) were synthesized with the goal of improving membrane anchoring and manipulating self-assembly. Monomeric and dimeric peptides, whether conjugated or not to a single lipophilic group, reduced infection *in vivo*. Bis-conjugation with lipophilic groups, in contrast, abrogated activity. Based on the physicochemical properties, self-assembly and membrane insertion kinetics of the HRC-L454W peptides we show that bis-conjugation increases the stability and order of the inner core of the spontaneously self-assembled nanoparticles, resulting in their compaction. The presence of the tryptophan residue also increases steric hindrance effects in the nanoparticle of the dimeric peptides, contributing to inter-peptide cluster meshing, but the same level of compaction is not achieved. We propose that the highly ordered packing and stability of molecular clusters forming the inner core of self-assembled nanoparticles prevent efficient dissociation of the peptides *in vivo*, hindering their release and therefore eliminating their antiviral efficacy.

Keywords: Nanoparticle; Self-assembling peptide; Self-assembly stability; Fusion-inhibitory peptide; Measles virus

Introduction

Recent developments in nanoscale engineering and molecular design have advanced the field of nanomedicine [1]. The possibility of controlling size, shape, and mechanical and biological properties of nanomaterials has enticed researchers to design nanomaterials targeted for diagnosis or therapy of several diseases [2-8]. Self-assembling peptides, usually composed of a biologically active peptide and a lipophilic "tail" group, are one promising class of compounds. In aqueous medium these peptides self-assemble into nanoparticles in which the lipophilic groups aggregate forming a hydrophobic core, and the peptide moieties are at the surface exposed to the solvent [9,10]. Nanoparticle architecture contributes to peptides' resistance to circulating proteases, enhancing biodistribution, while largely maintaining their target specificity compared to peptide monomers [11]. Nanoparticle design strategy is particularly attractive for peptide-based antiviral drugs, since pharmacological issues of antiviral peptides [12-14] such as low permeability across biological membranes and reduced half-life could be overcome.

Re-emergence of measles virus (MeV) infection and outbreaks, in part related to the spread of anti-vaccination views, has been a cause for concern, especially for infants and immunocompromised patients [15]. The need for chemotherapy is urgent and calls for innovative approaches against MeV [16,17]. Peptides derived from the C-terminal heptad repeat (HRC) of the MeV fusion protein (MeV-F) block the natural association between the HRC domains and the N-terminal heptad repeat (HRN) domains responsible for fusion of the viral and target cell membranes [18,19], inhibiting viral infectivity. HRC peptides have been modified by conjugation to lipophilic moieties, dimerization [20,21], and using polyethylene glycol (PEG) [22] as a flexible linker, to form self-assembling peptides. *In vivo* antiviral efficacy is modulated by the structural organization of the peptide nanoparticles. Monomers assembled into micellar stable nanoparticles are less prone to insert into lipid membranes, while dimers assemble into amorphous, loose, unstable nanoparticles, interacting more extensively with target membranes [17].

The leucine-to-tryptophan mutation at residue 454 of the MeV-F (L454W) was detected in a measles virus isolated during an outbreak in South Africa [23]. We have shown that the MeV-F bearing the

L454W residue has decreased thermal stability compared to F bearing L454 [24]. The presence of tryptophan (Trp) residues in membrane-active viral peptides enhances their activity [25]. Trp residues have a propensity to locate at the membrane interface [26], through a combined effect of size, rigidity and aromaticity. These properties stabilize the interaction of Trp-containing membrane proteins with lipid bilayers [27]. Trp residues act as anchors at interfaces and have a significant effect on conformation, stabilizing peptides and transmembrane protein segments in lipid bilayers. Given the positive correlation between nanoparticle instability, membrane interaction and *in vivo* antiviral efficacy of the HRC peptides, we hypothesized that the presence of the Trp residue could improve peptide antiviral efficiency. In this study we explored the structural stability of self-assembled nanoparticles and the membrane insertion kinetics of HRC peptides with Trp at residue 454 (HRC-L454W) and a set of derivatives (Table 1) to correlate these properties with *in vivo* efficacy. Antiviral efficacy *in vitro* and *in vivo* depends on a tradeoff between the advantageous aspects of nanoparticle assembly and the stability of molecular clustering in the nanoparticles, since very stable and orderly packed nanoparticles lose activity.

Material and Methods

Peptide synthesis

HRC-L454W peptides (HRC (1 to 8)-L454W) were produced by American Peptide Company (Sunnyvale, CA, USA) based on our design. Lipid moieties derivatives were custom synthesized by Charnwood Molecular (Loughborough, UK) based on our specifications. Peptides were synthesized by standard 9-fluorenylmethoxy carbonyl solid-phase methods, with the lipid moieties being attached to the peptides via a chemoselective reaction between the thiol group of an extra cysteine residue, added to the sequence C-terminal, and a bromoacetyl derivate of cholesterol (Chol)/tocopherol (Toc), or a bis-maleimide functionalized Chol/Toc core, interspaced by a tetra-polyethene glycol flexible linker [28-30].

Reagents and chemicals

The lipid 1-palmitoyl-2-oleyl-sn-glycero-3-phosphocholine (POPC) and sphingomyelin (SM) were purchased from Avanti Polar Lipids (Alabaster, AL, USA). Acrylamide, 1-anilino-8-naphthalenesulfonate (ANS), pyrene and Chol were obtained from Sigma-Aldrich (St. Louis, MO, USA). N-2-hydroxyethylpiperazine-N′-2-ethanesulfonic acid (HEPES), NaCl, dimethyl sulfoxide (DMSO), chlorophorm (the last two with spectroscopic grade) were purchased from Merck (Darmstadt, Germany).

Instrumentation

For steady-state and time-resolved fluorescence measurements a FLS920 series and LifeSpec II spectrofluorometers were used, respectively, both from Edinburgh Instruments (Livingston, UK). Dynamic light scattering (DLS) measurements were performed in a Malvern Instruments Zetasizer Nano ZS (Worcestershire, UK). Surface plasmon resonance (SPR) experiments were performed in a GE Healthcare Biacore X100 (Little Chalfont, UK). Extrusion of liposomal vesicles were carried out in a LiposoFast-Basic plus Stabilizer setup from Avestin (Mannheim, Germany) with Hamilton (Bonaduz, Switzerland) syringe through a 50 nm pore Nucleopore polycarbonate membrane (Whatman/GE Healthcare, UK).

Beta-Galactosidase complementation-based fusion assay

The beta-galactosidase (beta-gal) complementation-based fusion assay was performed as described previously [24]. Briefly, 293T cells transiently transfected with either Nectin-4 or CD150 (Table 2) and the omega reporter subunit (target cells) were incubated for the indicated period with cells co-expressing viral glycoproteins (H and F) and the alpha reporter subunit (effector cells), in the presence or absence of HRC-L454W fusion inhibitor peptide [31]. In the absence of peptides the fusion between the target and effector cells led to reconstitution of beta-galactosidase activity, quantified using a luminescence-based kit (Galacto-Star™ β-Galactosidase Reporter Gene, ThermoFisher, USA). In the presence of peptides fusion is reduced, reflected in a reduction in beta-gal activity. Data are from at least three independent experiments.

Infection analysis

To evaluate the effect of HRC-L454W peptides, cotton rats (CR) were inoculated intranasally (i.n.) with peptide (5 mg/kg in 100 μL of water) at 24 h and 12 h before infection. Four days after infection, the animals were asphyxiated using CO_2, and their lungs were collected and weighed. Lung tissue was minced with scissors and homogenized with a Dounce glass homogenizer. Serial 10-fold dilutions of supernatant fluids were assessed for the presence of infectious virus in a 48-well plate using cytopathic effect (CPE) in Vero cells expressing human CD150 (SLAM) as the endpoint. Plates were scored for CPE microscopically after 7 days. The amounts of virus in inocula were expressed as fold dilutions that resulted in the infection of 50% of inoculated tissue culture monolayers ($TCID_{50}$). The $TCID_{50}$ was calculated as described previously [32]. The animal experiments were approved by the Institutional Animal Care and Use Committee of Ohio State University.

Peptide	Sequence
HRC1-L454W	Ac-PPISWERLDVGTNLGNAIAKLEDAKELLESSDQILR-GSGSG-C-(CH_2CONH_2)-NH_2
HRC2-L454W	Ac-PPISWERLDVGTNLGNAIAKLEDAKELLESSDQILR-GSGSG-C-(PEG_4-Chol)-NH_2
HRC3-L454W	[Ac-PPISWERLDVGTNLGNAIAKLEDAKELLESSDQILR-GSGSG-C-(MAL-PEG_{11})-NH_2]$_2$
HRC4-L454W	[Ac-PPISWERLDVGTNLGNAIAKLEDAKELLESSDQILR-GSGSG-C-(MAL-PEG_4)NH_2]$_2$-Chol
HRC5-L454W	Ac-PPISWERLDVGTNLGNAIAKLEDAKELLESSDQILR-GSGSG-C-(PEG_4-Toc)-NH_2
HRC6-L454W	[Ac-PPISWERLDVGTNLGNAIAKLEDAKELLESSDQILR-GSGSG-C-(MAL-PEG_4)NH_2]$_2$-Toc
HRC7-L454W	Ac-PPISWERLDVGTNLGNAIAKLEDAKELLESSDQILR-GSGSG-C-[PEG_4-(Chol)$_2$]-NH_2
HRC8-L454W	Ac-PPISWERLDVGTNLGNAIAKLEDAKELLESSDQILR-GSGSG-C-[PEG4-(Toc)$_2$]-NH_2

Table 1: MeV-L454W HRC-derived peptides. The designed set of derivatives allows the comparative study of the effects of peptide dimerization (HRC1-L454W *vs* HRC3-L454W), mono-conjugation with lipophilic groups (HRC1-L454W *vs* HRC2-L454W, HRC1-L454W *vs* HRC5-L454W), bis-conjugation with lipophilic groups (HRC1-L454W *vs* HRC7-L454W, HRC1-L454W *vs* HRC8-L454W), combined effect of peptide dimerization and conjugation with lipophilic group (HRC3-L454W *vs* HRC4-L454W, HRC3-L454W *vs* HRC6-L454W), and chemical nature of the conjugated lipophilic groups (HRC4-L454W vs HRC6-L454W, HRC7-L454W *vs* HRC8-L454W). Ac, acetyl; Chol, cholesterol; MAL, maleimide; NH_2, amide; PEG_4, Tetra (ethylene glycol); Toc, tocopherol.

Peptide	Fusion inhibition at 24 h											
	Nectin-4						CD150					
	IC$_{50}$ (µM)			IC$_{90}$ (µM)			IC$_{50}$ (µM)			IC$_{90}$ (µM)		
HRC1-L454W	>10			ND			0.23	±	0.085	6	±	2
HRC2-L454W	0.37	±	0.02	2.3	±	0.3	0.01	±	0.002	0.23	±	0.07
HRC3-L454W	1.3	±	0.7	>10			0.04	±	0.01	1.8	±	0.1
HRC4-L454W	0.07	±	0.01	0.4	±	0	0.0013	±	0.0005	0.1	±	0
HRC5-L454W	1.9	±	0.07	>10			0.035	±	0.015	2.9	±	1
HRC6-L454W	8	±	2	>10			0.08	±	0.02	0.6	±	0
HRC7-L454W	>10			ND			>10			ND		
HRC8-L454W	>10			ND			>10			ND		

Table 2: HRC-L454W peptides *in vitro* efficacy at blocking fusion between 293T expressing MeV IC323 H+ F glycoproteins and 293T Nectin-4 or CD150, over 24 h.

Peptide solutions preparation

Lyophilized HRC-L454W peptides were first solubilized in DMSO to 10 mg/mL (except HRC4-L454W, which was 6 mg/mL), and after 5 min sonication, peptide stock solutions were divided into aliquots and stored at -20ºC. Peptide working samples were prepared with 10 mM HEPES buffer, 150 mM NaCl, pH 7.4 (sample buffer), to a final peptide concentration ranging from 2 to 10 µM, containing 2% (v/v) DMSO. Peptide samples were sonicated twice for 3 min prior to use.

ANS fluorescence studies

To monitor the aggregation of the HRC-L454W peptides, a 12.8 µM ANS solution in sample buffer was titrated with each peptide up to 10 µM. For each sample, after 10 min incubation, fluorescence emission spectra were collected between 400 and 600 nm, with the excitation wavelength (λ_{exc}) at 365 nm. Excitation and emission slits were 10 and 5 nm, respectively, with the temperature set at 25ºC. The fluorescence emission intensity values were corrected for dilution and background noise. The emission maximum wavelength (λ_{max}), and the spectrum integral ($\Sigma[I_F(\lambda)]$), were determined for each spectrum. Three independent replicates were performed for each sample.

Dynamic light scattering

DLS measurements were performed to determine the hydrodynamic radius (R_H) of the peptides nanoparticles. HRC-L454W peptide samples, from 2 to 10 µM, were prepared as described above and incubated for 5 min at 25ºC before each measurement. Measurements consisted of 10 individual runs, each corresponding to an averaged autocorrelation curve obtained from at least 10 repeated sample scans. Additionally, the kinetics of R_H variation at 10 µM were also registered. Measurements were performed in successive individual runs, after incubation periods of 5 min at 25ºC. The time interval between individual runs were 7.5 min, which corresponded to measurement time plus incubation time. Diffusion coefficient (D) values were collected for a total of 7.5 h. D values were calculated from autocorrelation curves using a CONTIN-based method [33]. D values were used to determine number-averaged R_H distributions through the Stokes-Einstein-Sutherland equation [34]. R_H values correspond to the statistical mode of each number-averaged R_H distribution. Three independent replicates were performed for each sample.

Pyrene fluorescence emission peak ratio (Critical Micellar Concentration determination)

To estimate the HRC-L454W peptides' critical micellar concentration (CMC), pyrene was added in a final concentration of 5 µM, from a 2.47 M stock solution in DMSO, to peptide samples in a range of concentrations from 0.01 to 10 µM. The final concentration

of DMSO was always lower than 2% (v/v). After 10 min incubation, fluorescence emission spectra were collected between 350 and 450 nm, with λ_{exc} at 330 nm, using excitation and emission slits of 4 and 2 nm, respectively, at 25ºC. Two emission intensity peaks were analyzed, I and III, which correspond to 372 and 383 nm, respectively. CMC values were obtained through the 3:1 ratio method: CMC corresponds to the inflection point in the plot of pyrene I_{III}/I_I ratio against peptide concentration. The X value of the intersection between the linear regression fit of the values before inflection and the linear regression fit of the values after the inflection correspond to the CMC value. Three independent replicates were performed for each peptide.

ANS fluorescence quenching by acrylamide

ANS fluorescence quenching by acrylamide studies were carried out by sequential addition of acrylamide (0-500 mM), to each HRC-L454W peptide sample at 10 µM, containing 12.8 µM ANS. After 10 min incubation, the peptide samples fluorescence emission spectra were collected between 400 and 600 nm, with the λ_{exc} at 365 nm, using excitation and emission slits of 10 and 5 nm, respectively, at 25ºC. The fluorescence emission intensity values were corrected for the dilution factor and background noise. Quenching data was fitted by the Stern-Volmer equation [35]:

$$\frac{I_0}{I} = 1 + K_{SV} \times [Q] \tag{1}$$

in which I_0 is the fluorescence intensity in the absence of quencher, I is the fluorescence intensity of each sample in the presence of the quencher at concentration $[Q]$, and K_{SV} is the Stern-Volmer constant. In case of a negative deviation in the Stern-Volmer plot, the quenching data was fitted by the Lehrer equation [35]:

$$\frac{I_0}{I} = \frac{1 + K_{SV}[Q]}{(1 + K_{SV}[Q])(1 - f_b) + f_b} \tag{2}$$

where f_b is the fraction of the light emitted by the peptide accessible to the quencher.

ANS time-resolved fluorescence decays were obtained using the laser excitation at λ_{exc} of 360 nm, with a stop condition of 10000 counts at the channel of maximal accumulation. Pre-exponentials factors (a_i) and fluorescence life-time values (τ_i) were obtained through fitting of the fluorescence decays with the software FAST. The amplitude average lifetime in the absence of the quencher (τ_0) was calculated by the equation [35]:

$$< \tau_0 > = \sum \frac{a_i \tau_i^2}{a_i \tau_i} \tag{3}$$

The bimolecular constant (k_q) values were calculated using the equation [35]:

$$<k_q> = \frac{K_{SV}}{<\tau_0>} \tag{4}$$

Surface plasmon resonance

To investigate the affinity of the HRC-L454W peptides towards lipid membranes, SPR experiments were performed. Small unilamellar vesicles (SUV) of POPC and POPC-Chol-SM (1:1:1) were used as membrane model systems and prepared as described elsewhere [36-38]. The lipids were solubilized in chloroform in a round-bottom flask and the organic solvent was evaporated under a gentle nitrogen flow, forming a thin lipidic film which was placed under vacuum overnight. The lipidic film was rehydrated with sample buffer and 10 freeze/thaw cycles were performed resulting in a suspension of multi-lamellar vesicles (MLV). SUV were obtained by extrusion of the MLV through 50 nm-pore size polycarbonate filters. Sample buffer containing 2% (v/v) DMSO was used as running buffer to match the peptide sample buffer composition. The flow system was primed three times before initiating an experiment. L1 sensor chips were used in all experiments. Each sensor chip was rinsed with three injections of 20 mM CHAPS before starting an assay. To prepare the lipid surface, 1 mM POPC or POPC-Chol-SM SUV sample was injected over the sensor chip at a 2 μL/min flow speed for 2400 s. Loosely bound vesicles were removed with a 36 s injection of 10 mM NaOH at 50 μL/min flow. HRC-L454W peptide samples at 10 μM, were injected over the deposited SUV surface at 5 μL/min flow speed during 200 s (association time). Each sample was allowed 800 s dissociation time after injection stopped. After each run, the L1 sensor chip was regenerated with sequential injections of 20 mM CHAPS (5 μL/min for 60 s), 0.5% (v/v) SDS (5 μL/min for 60 s), 10 mM NaOH containing 20% (v/v) methanol (50 μL/min for 36 s), and 10 mM NaOH (50 μL/min for 36 s). Response values were monitored to ensure effective surface regeneration. Response values were corrected for the peptide molecular weight. Three independent replicates were performed for each peptide.

Coarse-grained molecular dynamics simulations

HRC and HRC-L454W CG structures were built in three stages: (1) homology modeling was used to obtain the atomistic structures of the HRC and HRC-L454W peptides, based on the atomistic structure of the post-fusion human type 3 Parainfluenza Virus (hPIV3) fusion protein (PDB: 1ZTM), used as MeV-F model due to their structural homology [18,39,40]. The Martini model was used as the CG forcefield. The atomistic structures were converted to the corresponding CG models using the martinize.py script [41], for subsequent simulation under the GROMACS 5.1 package [42]; (2) a 4-unit PEG linker, built from an existing CG model of PEG [43] was appended to the peptides. To simplify the CG modeling maleimide was not taken into account and was instead replaced by three PEG beads in the final models (for a total 7-unit PEG linker); (3) for the Chol- and Toc-conjugated peptides the previously described Chol [44] or Toc [45] models were appended to the linker segment. Parameters for linker connections followed those of the Cys sidechain particle that they replaced.For the aggregation simulations, boxes containing 8 peptide molecules and either 23075 Martini waters, 271 Na+ and 255 Cl- molecules for monomeric peptides, or 23051 Martini waters, 295 Na+ and 255 Cl- molecules for dimeric peptides, were used. Each box had a neutral net charge and recreated the 150 mM *in vitro* solvent saline concentration. To prevent overestimation of the peptide association strength, a reported problem

of the Martini forcefield [41], peptide-water interaction forces were increased by 25% to allow peptides to associate and dissociate in the microsecond scale. Simulations were performed with 20 fs integration steps, for final trajectory durations of 10 μs. Temperature was coupled to 300 K using v-rescale thermostat with 1 ps coupling time, and the pressure was isotropically coupled to 1 bar using the Parrinello-Rahman barostat with a 12 ps coupling time.

Simulation analysis

Two analytical methods were used to differentiate the aggregation process of the peptides. Aggregation cluster was defined as a group of two or more peptides connected by their hydrophobic domains. For each simulation, the preferential interaction regions between pairs of peptides were mapped, and three different types of interactions were counted (HD-HD: interactions between hydrophobic domains; HD-P_A: interactions between a hydrophobic domain and a peptide chain in the same aggregation cluster, defined as a group of two or more peptides connected by their hydrophobic domains; HD-P_{A-A}: interactions between a hydrophobic domain and a peptide chain in different aggregation clusters). The aggregate cluster bridge ratio, R_{A-A}, was calculated through the following relationship:

$$R_{A-A} = \frac{t_{CGS}(HD-P_{A-A})}{t_{CGS}(HD-HD) + t_{CGS}(HD-P_A) + t_{CGS}(HD-P_{A-A})} \tag{5}$$

in which t_{CGS}(HD-HD), t_{CGS}(HD-P_A) and t_{CGS}(HD-P_{A-A}) correspond to the respective coarse-grained simulation contact times for each interaction type, quantified as a percentage of the total simulation time. Bootstrap method [46] was used to obtain the statistical error resulting of these procedures. These procedures were implemented in Python with extensive use of the MDAnalysis [47] and NumPy packages. Both analyses discarded the first 1 μs of initial trajectory time as peptide equilibration and approximation time. Visualization and image generation were carried out using the VMD 1.9.3 package [48] and the Tachyon ray-tracer. Peptide simulation movies are included in the Supplementary Information.
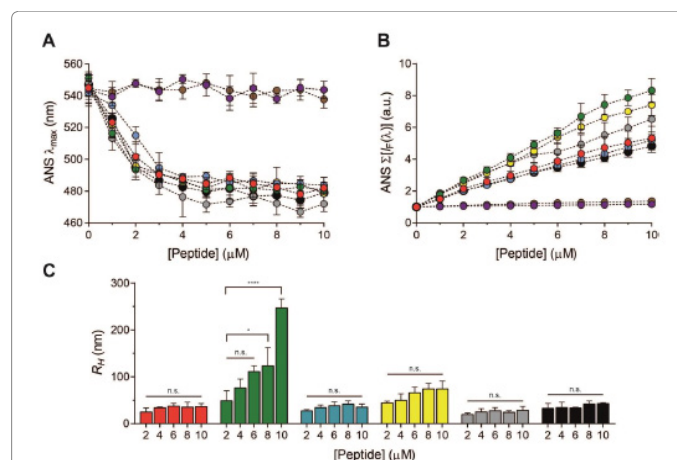
Results

HRC-L454W fusion-inhibition efficacy against MeV *in vitro* and *in vivo*

Inhibition of viral glycoprotein-mediated fusion was assessed in an *in vitro* fusion assay using 293T cell targets expressing either of the two known MeV receptors (CD150/SLAM and Nectin-4) (Table 2). We found this assay to be the most stringent *in vitro* method for quantitatively assessing inhibition. Effector cells transfected with H and F were allowed to fuse with target cells expressing either CD150/SLAM or Nectin-4 in the presence of the indicated peptide fusion inhibitors. After 24 h, fusion was evaluated using a beta-galactosidase complementation assay [24]. The IC$_{50}$ and IC$_{90}$ values are lower in the presence of CD150/SLAM bearing cells compared to cells bearing Nectin-4 (as we have previously observed). Conjugation of the peptides with either cholesterol (HRC2-L454W) or tocopherol (HRC5-L454W) increased fusion inhibition potency. Dimerization (HRC3-L454W, HRC4-L454W, and HRC6-L454W) also increased the activity as we previously reported [16,17]. The overall inhibitory values were higher than the corresponding HRC peptides bearing Leu at residue 454 but the overall profile was similar [17]. The addition of two lipid moieties to a peptide, either bis-cholesterol (HRC7-L454W) or bis-tocopherol (HRC8-L454W), abrogates the fusion inhibition activity.

Antiviral prophylactic efficacy for MeV *in vivo* was assessed in cotton rats (CR) as an infection model. The peptide antivirals were administered by intranasal delivery 24 and 12 h before infection. Four days after infection, the animals were euthanized and the viral titers in the animals' lungs were quantified. Treatment with HRC1 to 6-L454W peptides significantly reduced the viral titer in the lungs compared with the untreated control (Figure 1). In line with the unexpected *in vitro* results, HRC7 and -8-L454W peptides-treated animals had viral titers with no significant differences from those of the untreated animals, revealing poor antiviral activity against MeV *in vivo*. Previous results showed that after prophylaxis with the HRC peptides bearing L at position 454; HRC2, HRC3, HRC4 and HRC6 no MeV titer was detectable in the rats lungs suggesting that the *wt* HRC-derived sequence (L454) may have better inhibition activity [17]. Because self-assembly properties and membrane affinity modulate the antiviral efficacy of these peptides [17], alterations in these properties resulting from the Trp presence and/or the bis-conjugation strategy could explain the reduced efficacy of the bis-conjugated HRC7 and -8-L454W peptides. To explore this possibility, self-assembly and membrane interaction of the HRC-L454W peptides were studied.

Self-assembly properties of the lipid-conjugated HRC-L454W peptides

ANS is a small probe (~300 Da) that is highly fluorescent in apolar environments. ANS interacts non-specifically with hydrophobic pockets that result from molecular aggregation, increasing its fluorescence emission intensity. This is accompanied by a blue shift in the λ_{max} [49]. To study the self-assembly properties of HRC-L454W peptides, ANS fluorescence emission λ_{max} (Figure 2A) and intensity (Figure 2B) were measured in the presence of increasing concentrations of each peptide. A similar blue shift was observed for the lipid-conjugated peptides. The maximum shift was 64 nm on average, being constant for peptide concentrations above 5 μM. Increasing values of fluorescence intensity as a function of the lipid-conjugated peptide concentrations were detected. At 10 μM, for HRC2, -5 ,-7 and -8-L454W, the ANS fluorescence emission spectra integral ($\Sigma[I_F(\lambda)]$) was 5-fold higher than the control in the absence of peptide, while for HRC4 and -6-L454W, the ANS $\Sigma[I_F(\lambda)]$ was above 7.5-fold higher than the control. No significant ANS spectral shift or integrated emission intensity variation were observed for HRC1 and -3-L454W peptides. These results are in line with the conclusion that lipid-conjugated peptides aggregate into
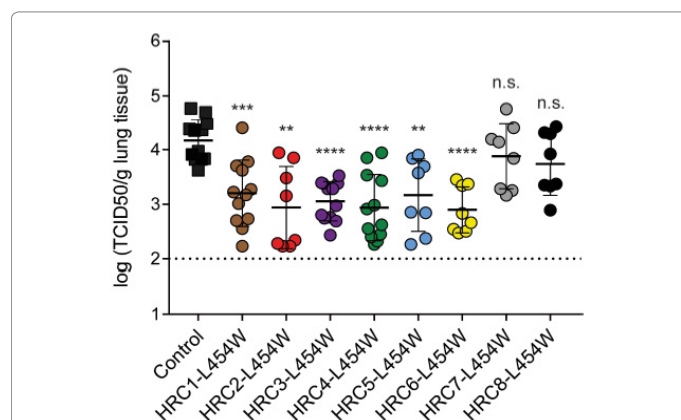

Figure 2: Self-assembly properties of the HRC-L454W peptides. λ_{max} (A) and the $\Sigma[I_F(\lambda)]$ (B) dependence on peptide concentration -(HRC1-L454W, brown; HRC2-L454W, red; HRC3-L454W, purple; HRC4-L454W, green; HRC5-L454W, blue; HRC6-L454W, yellow; HRC7-L454W, grey; HRC8-L454W, black). (C) Statistical mode of the number-averaged R_H distribution from DLS autocorrelation functions. The mean R_H values were compared using Tukey's method to test pairwise differences between concentrations of the same peptide (comparison to 2 μM is shown). Results correspond to the average of three independent replicates. Error bars represent the SD. n.s., not significant; *, P ≤ 0.01; ****, P ≤ 0.00001.

nanoparticles in solution, forming local hydrophobic pockets, while non-conjugated peptides do not self-assemble. Spectral variations registered between the lipid-conjugated peptides suggest differences in nanoparticle dimension and/or organization.

DLS is a technique that uses fluctuations in scattered light to measure the rate of diffusion of nanoscale particles, which in turn is used to determine dimensions of particles in solution [50]. Nanoparticles R_H were obtained for increasing concentrations of lipid-conjugated HRC-L454W peptides (Figure 2C). HRC2 -5, -7 and -8-L454W peptide self-assemble into smaller particles, with an R_H ranging from 32 to 43 nm, independent of the peptide concentration. This behavior is characteristic of stable and compact structures. In contrast, HRC4 and -6-L454W peptides self-assemble into nanoparticles with concentration-dependent dimensions, although not adequate for statistical significance in the case of HRC6-L454W. For HRC4-L454W nanoparticles there is a striking positive correlation between peptide concentration and particle dimension, which is indicative of a looser and unstable structure.

HRC-L454W nanoparticles have three different architectures

The ANS and DLS studies suggested variations in the internal structure of the self-assembled nanoparticles that may influence the *in vivo* inhibition efficacy of the HRC-L454W peptides. Focusing on this hypothesis, the apparent critical micellar concentration (CMC) was calculated based on pyrene fluorescence studies. Pyrene is a small fluorescent probe (~200 Da) very sensitive to environment polarity. In the presence of micellar nanoparticles, pyrene monomers penetrate into the hydrophobic interior of the nanoparticles, stacking into excimers. The pyrene emission spectrum is composed of five predominant vibronic bands. The intensity of the first band, the peak at 372 nm (I_I), is negatively affected by the formation of excimers, while the third band, at 383 nm (I_{III}), maintains its intensity independently of excimer formation [51]. The CMC value was obtained through the 3:1 intensity peak ratio method (Figure 3). Excimer formation only occurs in the presence of HRC2, -5, -7, -8-L454W micellar nanoparticles,
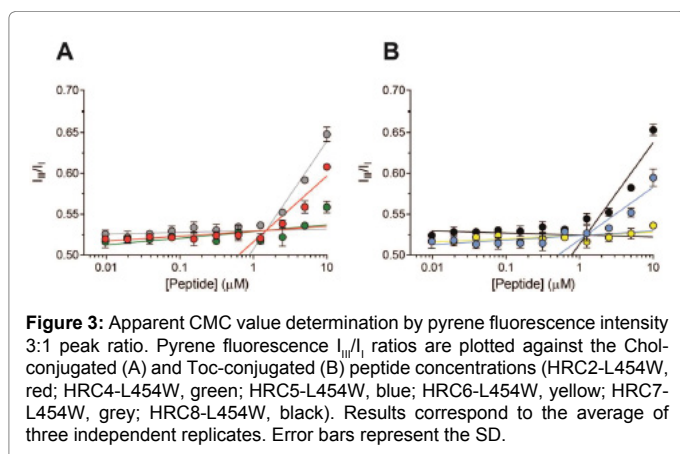

Figure 1: Intranasal administration of HRC-L454W peptides protects cotton rats from MeV infection. Mann-Whitney's method was used to compare viral titer reduction differences between the control animals and the treated animals. n.s., not significant; **, P ≤ 0.001; ***, P ≤ 0.0001; ****, P ≤ 0.00001.
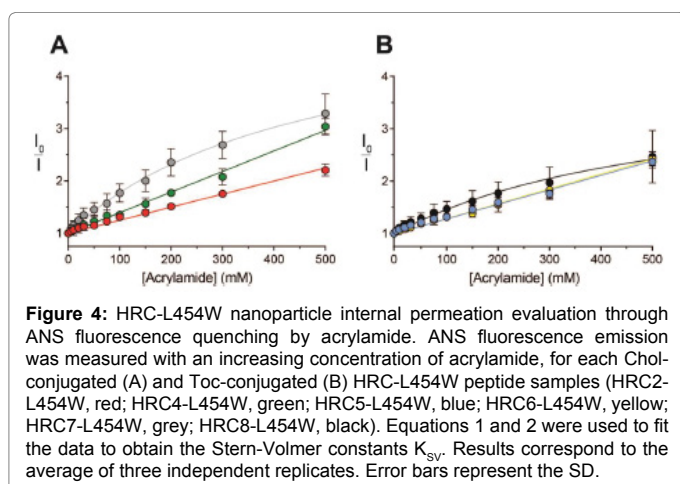
with an average CMC value of 1.45 μM. For HRC4 and -6-L454W, no pyrene spectral change is observed, suggesting that these peptides self-assemble into non-micellar amorphous nanoparticles.

In order to complement the pyrene fluorescence assays, nanoparticle internal packaging was also evaluated based on permeability to an aqueous solute. As described earlier, ANS non-specifically interacts with hydrophobic pockets that result from molecular aggregation. Acrylamide is an efficient neutral quencher soluble in aqueous solution. In loose, open, permeable ANS-trapping aggregates, acrylamide diffuses through the aggregate, quenching fluorescence emission from all ANS molecules. In compact micelle-like aggregates, acrylamide cannot reach the ANS in the inner core, therefore not being able to quench all fluorescence emission [27,52]. The $<k_q>$ values (Table 3), used as quantitative measure of quenching efficacy, are similar among HRC2, 5, and -6-L454W peptides, which reveals a general looseness of the nanoparticles formed by these peptides. Acrylamide quenching
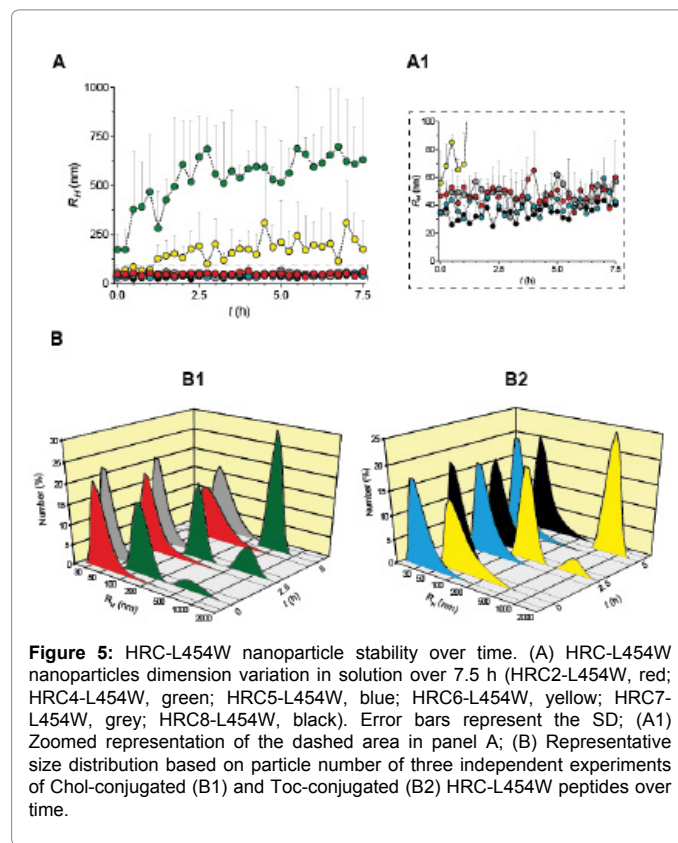
efficiency is higher in HRC4-L454W nanoparticles, when compared with the previous peptides, revealing a looser internal structure. In contrast with the other peptides, the downward curvature in the HRC7 and -8-L454W Stern-Volmer plots (Figure 4) reveals the existence of a non-accessible ANS sub-population - 18.6 and 25.2%, respectively - within the nanoparticles, which suggest that the addition of one more Chol/Toc domain per peptide contributes to a higher compaction of the nanoparticles hydrophobic cores, probably formed by interactions between these lipophilic domains. Interestingly, concomitant with this increased inner packaging, a 3-fold increase of the $<k_q>$ values relative to the other peptides is observed. This finding suggested that the solvent-accessible fractions of the HRC7 and -8-L454W nanoparticles - the spaces between the peptide chains - are more exposed and have a looser structure. To investigate this hypothesis, circular dichroism analysis was performed to determine the peptides' secondary structure (Supplementary Information Figure S1 and Table S1). HRC4, -7 and -8-L454W peptides had the lowest helical content, which is consistent with the peptide chains being highly exposed to the aqueous environment; hydrophobic shielding of the peptide chains promotes their helical conformation [53,54].

Figure 3: Apparent CMC value determination by pyrene fluorescence intensity 3:1 peak ratio. Pyrene fluorescence I_{III}/I_I ratios are plotted against the Chol-conjugated (A) and Toc-conjugated (B) peptide concentrations (HRC2-L454W, red; HRC4-L454W, green; HRC5-L454W, blue; HRC6-L454W, yellow; HRC7-L454W, grey; HRC8-L454W, black). Results correspond to the average of three independent replicates. Error bars represent the SD.

Figure 4: HRC-L454W nanoparticle internal permeation evaluation through ANS fluorescence quenching by acrylamide. ANS fluorescence emission was measured with an increasing concentration of acrylamide, for each Chol-conjugated (A) and Toc-conjugated (B) HRC-L454W peptide samples (HRC2-L454W, red; HRC4-L454W, green; HRC5-L454W, blue; HRC6-L454W, yellow; HRC7-L454W, grey; HRC8-L454W, black). Equations 1 and 2 were used to fit the data to obtain the Stern-Volmer constants K_{SV}. Results correspond to the average of three independent replicates. Error bars represent the SD.

Figure 5: HRC-L454W nanoparticle stability over time. (A) HRC-L454W nanoparticles dimension variation in solution over 7.5 h (HRC2-L454W, red; HRC4-L454W, green; HRC5-L454W, blue; HRC6-L454W, yellow; HRC7-L454W, grey; HRC8-L454W, black). Error bars represent the SD; (A1) Zoomed representation of the dashed area in panel A; (B) Representative size distribution based on particle number of three independent experiments of Chol-conjugated (B1) and Toc-conjugated (B2) HRC-L454W peptides over time.

Peptide	K_{SV} (M^{-1})			f_b	$<\tau_0>$ (ns)			$<k_q>$ (M^{-1} ns^{-1})
HRC2-L454W	2.497	±	0.05	-	7.793	±	0.033	0.32
HRC4-L454W	3.936	±	0.087	-	8.503	±	0.011	0.463
HRC5-L454W	2.77	±	0.065	-	6.945	±	0.095	0.399
HRC6-L454W	2.837	±	0.072	-	8.304	±	0.128	0.342
HRC7-L454W	11.58	±	1.3	0.814	8.49	±	0.37	1.364
HRC8-L454W	7.225	±	1.54	0.748	7.716	±	0.194	0.936

Table 3: ANS fluorescence emission quenching parameters in HRC-L454W self-assembled nanoparticles.

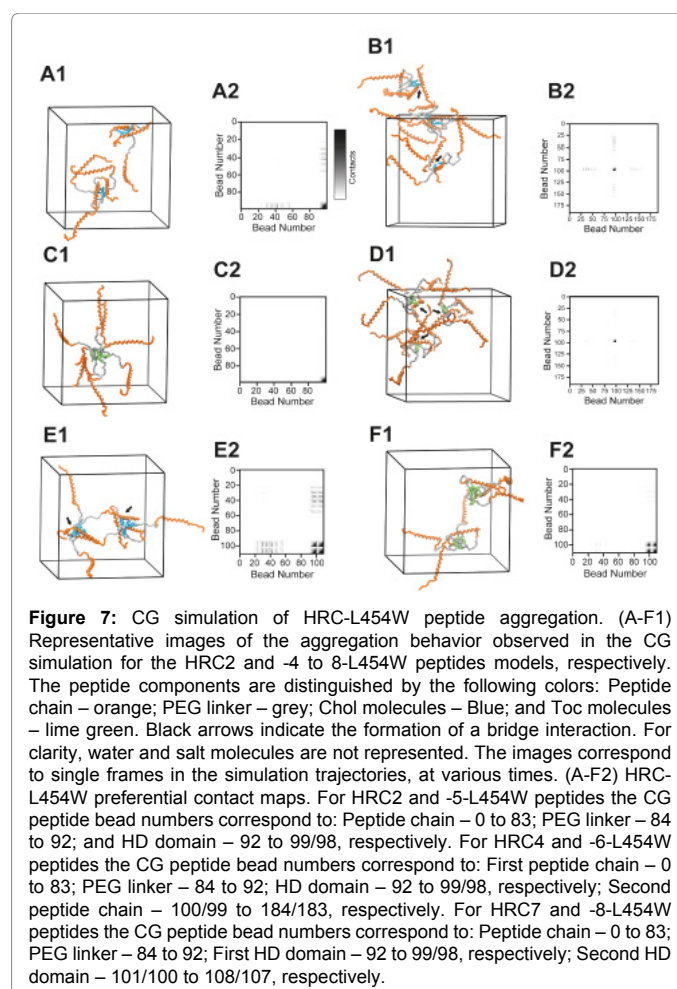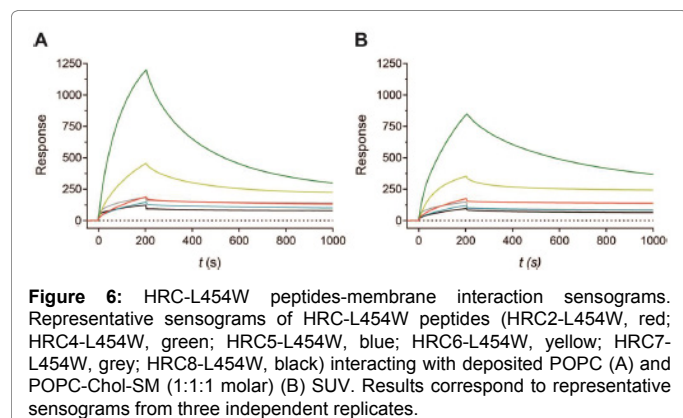## Monomeric peptides form stable nanoparticles in solution over time

Time-resolved DLS experiments were performed to further explore HRC-L454W nanoparticle stability. Nanoparticle size distributions were measured during 7.5 h in solution after preparation (Figure 5). The HRC2, -5, -7 and -8-L454W peptides formed a single and stable nanoparticle population over time, with no significant variations in their initial number-average R_H. In contrast, dimeric peptide nanoparticles grew over time. A bimodal population of nanoparticles was formed by the HRC4 and -6-L454W peptides. After 5 h, the larger size component became dominant. HRC6-L454W aggregates reach a maximum number-averaged R_H value of 310 nm, approximately 5-fold higher than the initial value, while HRC4-L454W aggregates reach a maximum average R_H of 697 nm, approximately 4-fold higher than the initial value.

HRC7 and -8-L454W do not insert into membranes

The efficacy of some fusion inhibitory peptides correlates with their capacity to insert in membranes [17,55,56]. SPR, a flow-based technique that allows real-time detection of molecular binding to a SUV-covered surface, was used to monitor peptide-membrane interactions [57]. SUVs were prepared with POPC to mimic cellular membranes or with POPC-SM-Chol (1:1:1) to mimic the Chol-enriched MeV membrane [58]. HRC4-L454W elicited the highest response upon interaction with the membranes of both lipid compositions, followed by HRC6-L454W, with half the response magnitude (Figure 6). HRC4 and -6-L454W particles unbind slowly from the surface, with a small fraction of the peptides remaining tightly bound to the SUV surface after total removal of peptide from the eluting buffer. Monomeric HRC-L454W has approximately 10-fold less the response values registered for HRC4-L454W. In contrast to the dimeric peptides, there was no slow release effect from the lipid surface observed for HRC2, -5, -7 and -8-L454W particles, indicating that the major fraction of the particles remain bound to the surface after passage of the eluting buffer.

Tryptophan substitution favors inter-cluster interactions in the dimeric HRC-L454W peptide aggregation process

The molecular level effects of the Leu-to-Trp substitution in the self-assembly process remained unclear after the experiments above. We had previously shown that CG molecular dynamics can capture important features of inter-molecular association during the aggregation process of HRC5 and HRC6 peptides in a μs range timescale [45]. The same CG methodology was used to analyze the assembly of the HRC-L454W peptides. HRC2 and HRC4 self-assembly mechanisms

Figure 6: HRC-L454W peptides-membrane interaction sensograms. Representative sensograms of HRC-L454W peptides (HRC2-L454W, red; HRC4-L454W, green; HRC5-L454W, blue; HRC6-L454W, yellow; HRC7-L454W, grey; HRC8-L454W, black) interacting with deposited POPC (A) and POPC-Chol-SM (1:1:1 molar) (B) SUV. Results correspond to representative sensograms from three independent replicates.

Figure 7: CG simulation of HRC-L454W peptide aggregation. (A-F1) Representative images of the aggregation behavior observed in the CG simulation for the HRC2 and -4 to 8-L454W peptides models, respectively. The peptide components are distinguished by the following colors: Peptide chain – orange; PEG linker – grey; Chol molecules – Blue; and Toc molecules – lime green. Black arrows indicate the formation of a bridge interaction. For clarity, water and salt molecules are not represented. The images correspond to single frames in the simulation trajectories, at various times. (A-F2) HRC-L454W preferential contact maps. For HRC2 and -5-L454W peptides the CG peptide bead numbers correspond to: Peptide chain – 0 to 83; PEG linker – 84 to 92; and HD domain – 92 to 99/98, respectively. For HRC4 and -6-L454W peptides the CG peptide bead numbers correspond to: Peptide chain – 0 to 83; PEG linker – 84 to 92; HD domain – 92 to 99/98, respectively; Second peptide chain – 100/99 to 184/183, respectively. For HRC7 and -8-L454W peptides the CG peptide bead numbers correspond to: Peptide chain – 0 to 83; PEG linker – 84 to 92; First HD domain – 92 to 99/98, respectively; Second HD domain – 101/100 to 108/107, respectively.

were also simulated, which allowed for comparison of HRC-L454 and HRC-L454W to assess the effect of Trp at this position. As described in Materials and Methods, in addition to trajectory examination, two procedures were used to complement the data analysis - preferential contact mapping and contact counting.

HRC2 and -5-L454W displayed a similar behavior during the simulations (Figure 7A and C): quick association of the peptides, preferentially by interactions between the lipophilic domains of 4-8 peptides. These formed aggregation clusters, were stable and long-lasting during almost the entire course of the simulation. Interactions were also observed between the lipophilic domain molecules and hydrophobic residues of the peptide chains - with higher occurrence in the HRC2-L454W simulation - although they only occur within the same aggregation cluster. In contrast, HRC4 and -6-L454W assembled into unstable and smaller aggregation clusters composed of 2-4 peptides (Figure 7B and D). Peptide interchange between clusters was observed continuously during the simulation trajectory. Bridge contacts between different clusters - defined as inter-cluster interactions between peptides and lipophilic moieties - occurred frequently. These interactions favor the formation of an unstable cluster network, in agreement with the *in vitro* observations. Contact maps highlight that Chol-Chol and Toc-Toc interactions were still preferential. However, interactions between the lipophilic domain and the peptide backbone of the HRC4 and -6-L454W increased compared to those registered for the HRC2 and -5-L454W peptides, respectively. Like the monomeric

peptides, the HRC7 and -8-L454W peptides assembled into stable and long-lasting aggregation clusters composed of 3-5 peptides (Figure 7E and F). Comparing these with the HRC2 and -5-L454W peptides, there is an increase in the interactions between the peptide backbone and the Chol and Toc molecules. Bridging interactions are a rare event in the HRC8-L454W simulation. One bridge interaction does occur throughout the HRC7-L454W simulation but does not, however, jeopardize the cluster's stability.

Through contact counting analysis (Table 4), we quantified the aggregate bridge ratio (R_{A-A}). As described, this parameter corresponds to the simulation time involved in bridge interactions as a fraction of the total interaction time and has been shown to correlate with aggregation instability [45]. Here, it was employed to quantitatively characterize the HRC and HRC-L454W peptide aggregation processes and explain their differences. In both groups of peptides, the R_{A-A} was ~0% for the mono-tagged monomeric peptides - expected due to their nanoparticle stability - while dimeric peptides had an increased R_{A-A}. However, the R_{A-A} measured for HRC4-L454W was 2-fold higher than for the HRC4 peptides, 21% and 11%, respectively, while the HRC6-L454W R_{A-A} was 3.5-fold higher than those registered for the HRC6, 17.1% and 5%, respectively. These values suggest a higher degree of aggregation instability for the peptides bearing a Trp at residue 454.

Another key finding was that dimeric Chol-conjugated peptides had an increased R_{A-A} compared to the dimeric Toc-conjugated ones, in agreement with the HRC-L454W experimental results. HRC7-L454W displayed an increased R_{A-A} value of 27.5 %, which in this particular case does not represent instability of the aggregation process, but rather the formation of the single stable bridge interaction. HRC8-L454W, similarly to the monomeric peptides, had a low R_{A-A} of 1.7%.

Discussion

Amphiphilic lipid-conjugated antiviral peptides are a promising class of molecules for the treatment of several viral infections [20,31,59]. Their ability to self-assemble into nanoparticles is expected to enhance biodistribution and self-delivery into sites of infection. Fusion inhibitor HRC peptides have previously been shown to have antiviral activity against MeV infection, and balance between self-assembly and membrane integration was key for optimizing antiviral effect. HRC peptides with a Trp at residue 454 (HRC-L454W) were now designed

in an effort to improve the fusion inhibition activity of HRC peptides. The amphiphilicity and self-assembling instability promoted by this residue were anticipated to improve anti-fusion effects. Evaluation of these peptides allowed for an investigation of the role of nanoparticle stability in the antiviral action of amphiphilic lipid-conjugated antiviral peptides.

HRC-L454W peptides blocked viral fusion *in vitro* and reduced MeV infection in cotton rat models, except for HRC7 and 8-L454W.

The biophysical characterization performed here shows that conjugated HRC-L454W peptides self-assemble into nanoparticles with three different architectures (Figure 8) that modulate peptide-membrane affinity. HRC2 and -5-L454W nanoparticles have a micelle-like compact structure with reduced dimensions, and are stable in solution as a result of Chol-Chol and Toc-Toc preferential interactions. These structures had low affinity towards lipidic membranes, because their stability does not allow efficient peptide dissociation from the nanoparticle clusters and insertion into the membranes. HRC4 and -6-L454W nanoparticles are amorphous, large and unstable structures. Peptide dimerization destabilizes the aggregation clusters of the particles, increasing bridging between small aggregates. Continuous clustering of unstable smaller particles in solution leads to prolonged growth of the aggregates and transformation of a metastable nanoparticle structure into a disorganized peptide web. This new structure favors interaction with lipids and insertion into membranes with prolonged residence times.
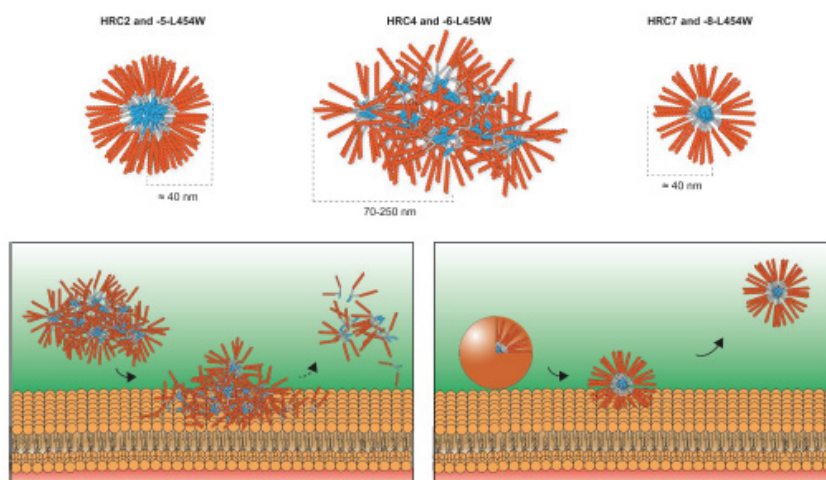
The hydrophobicity of Chol, compared to Toc favored contacts between the peptide backbone and the lipophilic molecules, contributing to the increased bridge formation observed in the simulation of these structures, which correlated with the increased R_H of the HRC4-L454W particles. Finally, HRC7 and -8-L454W self-assemble into micelle-like stable structures with reduced dimensions. In contrast with HRC2 and -5-L454W, there is greater compaction of the central hydrophobic core of the HRC7 and -8-L454W nanoparticles, in agreement with the double conjugation of each peptide to two hydrophobic groups. Stacking twice the Chol or Toc moieties in a nanoparticle of nearly the same size results in higher core density and probably in an expanded hydrophobic core volume. As a result, it is plausible that peptide chains are more widely separated from one another and therefore more permeable to the solvent and less restricted in conformation.

Peptide	t_{CGS} (%)				R_{A-A}
	No Contacts	HD-HD	HD-P$_A$	HD-P$_{A-A}$	
HRC2	55.1 ± 0.2	29.6 ± 0.2	14.6 ± 0.2	0.7 ± 0.1	1.5 ± 0.1
HRC4	67.0 ± 0.4	19.9 ± 0.3	10.0 ± 0.1	3.2 ± 3.2	11.1 ± 0.4
HRC5*	9.0 ± 0.5	90.1 ± 0.5	0.9 ± 0.1	0.0 ± 0.0	0.1 ± 0.01
HRC6*	67.1 ± 17.3	31.5 ± 8.4	0.5 ± 0.2	0.9 ± 0.3	5.0 ± 1.6
HRC2-L454W	54.4 ± 0.1	28.8 ± 0.2	16.7 ± 0.1	0.04 ± 0.01	0.1 ± 0.03
HRC4-L454W	79.2 ± 0.3	9.8 ± 0.3	7.2 ± 0.1	3.8 ± 0.1	21.0 ± 0.8
HRC5-L454W	11.2 ± 0.6	87.4 ± 0.7	1.3 ± 0.1	0.1 ± 0.02	0.2 ± 0.05
HRC6-L454W	88.8 ± 0.3	9.0 ± 0.3	0.8 ± 0.1	1.4 ± 0.1	17.1 ± 1.0
HRC7-L454W	44.6 ± 0.07	30.1 ± 0.05	10.1 ± 0.03	15.1 ± 0.04	27.5 ± 0.07
HRC8-L454W	56.9 ± 0.17	38.8 ± 0.2	3.6 ± 0.13	0.7 ± 0.08	1.7 ± 0.2

*Values described in the reference 45

Table 4: HRC and HRC-L454W CG simulations contacts counting analysis.

Figure 8: (Top) Simplified schematic representation of the structural organization of nanoparticles formed by the HRC-L454W peptides. (Bottom) Interaction of HRC-L454W aggregates with lipid membranes. Left Panel: Dimeric peptides organized in a peptide web cluster structure that allows efficient release and partition into the biological membranes' surface. Right Panel: Bis-conjugated nanoparticles are stable and compact, suppressing the peptides' release from the inner core, hindering efficient interaction with biological membranes.

The Trp residue at 454 in place of Leu rendered the dimeric peptide nanoparticles more unstable. We have shown that, at a molecular level, the Trp also increases steric hindrance effects in the aggregates due to its size and chemical structure. Incorrect Trp-Trp coupling, due to suboptimal geometrical interaction between the residues, destabilizes certain proteins [60-62]. The MeV-F protein bearing the L454W mutation indeed had decreased thermal stability [31]. Given the instability and disorder in the aggregation cluster system, HRC-L454W dimeric peptides have higher tendency to form intermolecular bridges. In addition, the Trp had no significant destabilizing effects on the monomeric nanoparticles. The higher degree of stability characteristic of these structures withstands the potential destabilizing effects of the Trp in place of Leu at residue 454. In contrast to initial expectations, the presence of the Trp residue did not improve the peptides' affinity towards membranes or their antiviral activity.

We have shown that self-assembled particle stability has a pivotal role in the *in vivo* action of amphiphilic lipid-conjugated antiviral peptides. The ability of the peptides to dissociate from the nanoparticle cluster structure and partition to biological membranes, in a slow-release effect, is a determinant of their distribution on the cell surface and efficacy *in vivo* (Figure 8). Despite the stability displayed by the HRC2 and -5-L454W nanoparticles in solution, they reduced viral titer during MeV infection in the cotton rat *in vivo*, suggesting that peptides are released from the nanoparticle clusters. Dimeric peptides HRC4 and -6-L454W self-assemble into unstable and disorganized structures, which resulted in an efficient interaction with biological membranes with high residence times, inhibiting MeV infection *in vivo*. In contrast, the bis-conjugated HRC7 and -8-L454W lost had little antiviral efficacy against MeV *in vivo*. Bis-conjugation increased the stability of the nanoparticles' inner core. We speculate that this structural stability prevented the efficient release of the peptides *in vivo* that is essential for the peptides to reach and inhibit their biological target, even in the presence of proteolytic agents present in the animal serum. Our results point towards the conclusion that stability of drug nanoparticles modulates antiviral efficacy in vivo and that a threshold exists above which stability decreases efficacy.

References

1. Chang EH, Harford JB, Eaton MAW, Boisseau PM, Dube A, et al. (2015) Nanomedicine: Past, present and future - A global perspective. Biochem Biophys Res Commun 68: 511-517.

2. Mitragotri S, Lahann J (2009) Physical approaches to biomaterial design. Nat Mater 8: 15-23.

3. López-Sagaseta J, Malito E, Rappuoli R, Bottomley MJ (2016) Self-assembling protein nanoparticles in the design of vaccines. Comput Struct Biotechnol J 14: 58-68.

4. Karmali PP, Kotamraju VR, Kastantin M, Black M, Missirlis D, et al. (2009) Targeting of albumin-embedded paclitaxel nanoparticles to tumors. Nanomedicine Nanotechnology Biol Med 5: 73-82.

5. Chung EJ, Tirrell M (2015) Recent Advances in Targeted, Self-Assembling Nanoparticles to Address Vascular Damage Due to Atherosclerosis. Adv Healthc Mater 4: 2408-2422.

6. Kanekiyo M, Wei CJ, Yassine HM, McTamney PM, Boyington JC, et al. (2013) Self-assembling influenza nanoparticle vaccines elicit broadly neutralizing H1N1 antibodies. Nature 499: 102-106.

7. Liu LH, Xu KJ, Wang HY, Tan PKJ, Fan WM, et al. (2009) Self-assembled cationic peptide nanoparticles as an efficient antimicrobial agent. Nat Nanotechnol 4: 457-463.

8. Zhang L, Pornpattananangkul D, Hu CM, Huang CM (2010) Development of Nanoparticles for Antimicrobial Drug Delivery. Curr Med Chem 17: 585-594.

9. Lakshmanan A, Zhang S, Hauser CAE (2012) Short self-assembling peptides as building blocks for modern nanodevices. Trends Biotechnol 30: 155-165.

10. Dehsorkhi A, Castelletto V, Hamley IW (2014) Self-assembling amphiphilic peptides. J Pept Sci 20: 453-467.

11. Chung EJ, Mlinar LB, Sugimoto MJ, Nord K, Roman BB, et al. (2015) In vivo biodistribution and clearance of peptide amphiphile micelles. Nanomedicine Nanotechnology Biol Med 11: 479-487.

12. Berkhout B, Eggink D, Sanders RW (2012) Is there a future for antiviral fusion inhibitors? Curr Opin Virol 2: 50-59.

13. Craik DJ, Fairlie DP, Liras S, Price D (2013) The Future of Peptide-based Drugs. Chem Biol Drug Des 81: 136-147.

14. Fosgerau K, Hoffmann T (2015) Peptide therapeutics: Current status and future directions. Drug Discov Today 20: 122-128.

15. Abad CL, Safdar N (2015) The Reemergence of Measles. Curr Infect Dis Rep 17: 51.

16. Welsch JC, Talekar A, Mathieu C, Pessi A, Moscona A, et al. (2013) Fatal Measles Virus Infection Prevented by Brain-Penetrant Fusion Inhibitors. J Virol 87: 13785-13794.

17. Figueira TN, Palermo LM, Veiga AS, Huey D, Alabi CA, et al. (2017) In Vivo Efficacy of Measles Virus Fusion Protein-Derived Peptides Is Modulated by the Properties of Self-Assembly and Membrane Residence. J Virol 91: e01554-16.

18. Plattet P, Alves L, Herren M, Aguilar HC (2016) Measles virus fusion protein: Structure, function and inhibition. Viruses 8: 112.

19. Laksono BM, De Vries RD, Mcquaid S, Duprex WP, De Swart RL, et al. (2016) Measles Virus Host Invasion and Pathogenesis. Viruses 8: 1-13.

20. Pessi A, Langella A, Capitò E, Ghezzi S, Vicenzi E, et al. (2012) A General Strategy to Endow Natural Fusion-protein-Derived Peptides with Potent Antiviral Activity. PLoS One 7: e36833.

21. Pessi A (2015) Cholesterol-conjugated peptide antivirals: a path to a rapid response to emerging viral diseases. J Pept Sci 21: 379-386.

22. Otsuka H, Nagasaki Y, Kataoka K (2012) PEGylated nanoparticles for biological and pharmaceutical applications. Adv Drug Deliv Rev 64: 246-255.

23. Hardie DR, Albertyn C, Heckmann JM, Smuts HEM (2013) Molecular characterisation of virus in the brains of patients with measles inclusion body encephalitis (MIBE). Virol J 10: 283.

24. Jurgens EM, Mathieu C, Palermo LM, Hardie D, Horvat B, et al. (2015) Measles fusion machinery is dysregulated in neuropathogenic variants. MBio 6: e02528-14.

25. Melo MN, Sousa FJR, Carneiro FA, Castanho MARB, Valente AP, et al. (2009) Interaction of the Dengue Virus Fusion Peptide with Membranes Assessed by NMR: The Essential Role of the Envelope Protein Trp101 for Membrane Fusion. J Mol Biol 392: 736-746.

26. Wimley WC, White SH (1996) Experimentally determined hydrophobicity scale for proteins at membrane interfaces. Nat Struct Biol 3: 842-848.

27. Liu W, Caffrey M (2006) Interactions of tryptophan, tryptophan peptides, and tryptophan alkyl esters at curved membrane interfaces. Biochemistry 45: 11713-11726.

28. Eckert DM, Kim PS (2001) Membrane of Viral Membrane Fusion and Its Inhibittion. Annu Rev Biochem 70: 777-810.

29. White JM, Delos SE, Brecher M, Schornberg K (2008) Structures and mechanisms of viral membrane fusion proteins: multiple variations on a common theme. Crit Rev Biochem Mol Biol 43: 189-219.

30. Sapir A, Avinoam O, Podbilewicz B, Chernomordik LV (2008) Viral and Developmental Cell Fusion Mechanisms: Conservation and Divergence. Dev Cell 14: 11-21.

31. Mathieu C, Huey D, Jurgens E, Welsch JC, DeVito I, et al. (2015) Prevention of Measles Virus Infection by Intranasal Delivery of Fusion Inhibitor Peptides. J Virol 89: 1143-1155.

32. Pfeuffer J, Puschel K, Meulen VV, Schneider-Schaulies J, Niewiesk S (2003) Extent of measles virus spread and immune suppression differentiates between wild-type and vaccine strains in the cotton rat model (Sigmodon hispidus). J Virol 77: 150-158.

33. Provencher SW (1982) Contin : a General Purpose Constrained Regularization Program for Inverting Noisy Linear Algebraic and Integral Equations. Elsevier 27: 229-242.

34. Berne BJ, Pecora R (2000) Dynamic Light Scattering: With Applications to Chemistry, Biology, and Physics. Dover Publications Inc.

35. Lakowicz JR (2013) Principles of Fluorescence Spetroscopy. (3rd edtn) Springer Berlin Heidelberg.

36. Olson F, Hunt CA, Szoka FC, Vail WJ, Papahadjopoulos D (1979) Preparation of liposomes of defined size distribution by extrusion through polycarbonate membranes. BBA Biomembr 557: 9-23.

37. Vemuri S, Rhodes CT (1995) Preparation and characterization of liposomes as therapeutic delivery systems: a review. Pharm Acta Helv 70: 95-111.

38. Santos NC, Castanho MARB (2002) Liposomes: has the magic bullet hit the target? Quim Nova 25: 1181-1185.

39. Plemper RK, Brindley MA, Iorio RM (2011) Structural and mechanistic studies of measles virus illuminate paramyxovirus entry. PLoS Pathog 7: 1-6.

40. Hashiguchi T, Fukuda Y, Matsuoka R, Kuroda D, Kubota M, et al. (2018) Structures of the prefusion form of measles virus fusion protein in complex with inhibitors. Proc Natl Acad Sci 201718957.

41. Jong DH De, Singh G, Bennett WFD, Wassenaar T, Sch L V, et al. (2012) Improved Parameters For F or The Martini Coarse- Coarse - Grained Protein Force Field. J Chem Theory Comput 9: 687-697.

42. Berendsen HJC, van der Spoel D, van Drunen R (1995) GROMACS: A message-passing parallel molecular dynamics implementation. Comput Phys Commun 91: 43-56.

43. Lee H, Vries AH De, Marrink S, Pastor RW (2009) A coarse-grained model for polyethylene oxide : conformation and hydrodynamics. Blood 13186-13194.

44. Melo MN, Ingólfsson HI, Marrink SJ (2015) Parameters for Martini sterols and hopanoids based on a virtual-site description. J Chem Phys 143: 243152-244118.

45. Figueira TN, Mendonça DA, Gaspar D, Melo MN, Moscona A, et al. (2018) Structure-Stability-Function Mechanistic Links in the Anti-Measles Virus Action of Tocopherol-Derivatized Peptide Nanoparticles. ACS Nano 12: 9855-9865.

46. Efron B, Tibshirani R (1986) Bootstrap Methods for Standard Errors, Confidence Intervals, and Other Measures of Statistical Accuracy. Stat Sci 1: 77-77.

47. Michaud-Agrawal N, Denning EJ, Woolf TB, Beckstein O (2011) MDAnalysis: A Toolkit for Analysis of Molecular Dynamics Simulations. J Comput Chem 32: 2319-2327.

48. Humphrey W, Dalke A, Schulten K (1996) VMD: Visual molecular dynamics. J Mol Graph 14: 33-38.

49. Hawe A, Sutter M, Jiskoot W (2008) Extrinsic fluorescent dyes as tools for protein characterization. Pharm Res 25: 1487-1499.

50. Brar SK, Verma M (2011) Measurement of nanoparticles by light-scattering techniques. TrAC Trends Anal Chem 30: 4-17.

51. Thomas JK, Kalyanasundara K (1977) Environmental effects on vibronic band intensities in pyrene monomer fluorescence and their application in studies of micellar systems. J Am Chem Soc 2039: 2039-2044.

52. Tovar JD, Claussen RC, Stupp SI (2005) Probing the interior of peptide amphiphile supramolecular aggregates. J Am Chem Soc 127: 7337-7345.

53. Zhong L, Johnson WC (1992) Environment affects amino acid preference for secondary structure. Proc Natl Acad Sci 89: 4462-4465.

54. Dill KA, Bromberg S, Yue K, Chan HS, Ftebig KM, et al. (2008) Principles of protein folding - A perspective from simple exact models. Protein Sci 4: 561-602.

55. Veiga AS, Santos NC, Loura LMS, Fedorov A, Castanho MARB (2004) HIV fusion inhibitor peptide T-1249 is able to insert or adsorb to lipidic bilayers. Putative correlation with improved efficiency. J Am Chem Soc 126: 14758-14763.

56. Franquelim HG, Loura LMS, Santos NC, Castanho MARB (2008) Sifuvirtide screens rigid membrane surfaces. Establishment of a correlation between efficacy and membrane domain selectivity among HIV fusion inhibitor peptides. J Am Chem Soc 130: 6215-6223.

57. Figueira TN, Freire JM, Cunha-santos C, Castanho MARB (2017) Quantitative analysis of molecular partition towards lipid membranes using surface plasmon resonance. Nat Publ Gr 1-10.

58. Vincent S, Gerlier D, Manie SN (2000) Measles virus assembly within membrane rafts. J Virol 74: 9911-9915.

59. Montero A, Gastaminza P, Law M, Cheng G, Chisari FV, et al. (2011) Self-Assembling Peptide Nanotubes with Antiviral Activity against Hepatitis C Virus. Chem Biol 18: 1453-1462.

60. Tatko CD, Waters ML (2009) The geometry and efficacy of cation-π interactions in a diagonal position of a designed β-hairpin. Protein Sci 12: 2443-2452.

61. Wu L, Mcelheny D, Huang R, Keiderling TA (2009) Role of Tryptophan-Tryptophan Interactions in Trpzip β-Hairpin Formation, Structure and Stability. Biochemistry 48: 10362-10371.

62. Waters ML (2004) Aromatic interactions in peptides: Impact on structure and function. Biopolym Pept Sci Sect 76: 435-445.